7. ATTITUDE RECONSTRUCTION

The attitude reconstruction turned out to be one of the most complex and challenging data reduction tasks, not least due to the complications caused by the elliptical orbit the satellite was forced to use and the resulting torque variations. There were also disturbances caused by the radiation received while passing through the van Allen belts, both direct (increased background levels in the star mapper detectors, preventing the recognition of signals) and indirect (damage to the gyro electronics and the on-board computer). In the reconstruction of the attitude the two consortia proceeded along very different strategies, both having their advantages and disadvantages. Generally, they were both designed to achieve the accuracy required for the reduction of Hipparcos data at the great circle level. The FAST method turned out to be more stable in particular near thruster firings, while the NDAC method was better equipped to deal with the more extreme behaviour (such as torques near perigee, gyro tests and accidental hits). Comparisons showed good agreement between attitudes computed by both methods even in the most difficult cases and both produced results well within the specifications.

7.1. The Attitude Reconstruction Problem

The aim of the attitude reconstruction was the determination of the attitude of a telescope reference frame as defined by the star mapper grid calibrations. The accuracy required by the Hipparcos mission was a standard deviation of the error better than 0.1 arcsec. During further processing in the great-circle reductions the along-scan attitude was further improved to a standard deviation of a few mas, which was acceptable also for the Tycho data reductions.

The on-ground attitude reconstruction was a very complex task and it is not possible in this short chapter to present in detail all the work done by the two consortia, which adopted different attitude models and different estimation procedures. The aim of this chapter is to present in a compact way the main lines of the estimation methodology followed, the assumptions introduced, and the quality of the results obtained.

Data Available for the Reconstruction of the Attitude

The attitude reconstruction relied primarily on the star mapper transit time determinations, described in Chapter 6. It also required the timings and lengths of the thruster

firings in order to recognise sudden changes in rotation rates and in order to provide boundary conditions linking data intervals between thruster firings. Other data sources available were the real-time attitude determination, providing the on-board estimates of the orientation and rotation rates of the satellite, and the gyro data, providing a constant record of the rotation rates. The gyro data and the real-time attitude determination were partly correlated. For the final attitude reconstruction results from the great-circle reductions could also be used.

The star mapper data stream, an average of one star every 4 seconds, was regularly interrupted for a period of 200 to 1000 seconds because of an occultation by the Earth or the Moon: shutters were closed when the image of the Earth or the Moon came too close to one of the fields of view. As no image dissector tube data was collected over these intervals either, there was no need for a reconstructed attitude over those intervals. Collection of gyro data continued during these intervals. Occultations were particularly long when the satellite was close to perigee.

Reconstructed attitude data was required for the processing of the image dissector tube data (see Chapter 5) and for the great-circle reductions (see Chapter 9). The required accuracy was 0.1 arcsec, and was set by great-circle reduction requirements. The accuracy of the rotation rates and the acceleration around the spin axis could influence the image dissector tube reductions, in particular for brighter stars (see Chapter 5). The attitude was also required for the Tycho data processing, which benefitted from the higher accuracy that was in fact obtained (see also Volume 4).

Principles of the Attitude Reconstruction

The attitude is given by three angles, suitably defined, which are semi-independent time functions. In the attitude reconstruction process three fundamental steps can be outlined: the attitude modelling, the attitude estimation and the hypothesis verification.

The attitude modelling is the step in which the attitude angles were defined and their variability in time was modelled by a finite set of unknown variables (degrees of freedom). Since in the most general case the above time functions presented an infinite continuous set of degrees of freedom, the attitude modelling had to introduce an approximation of the reality motivated by physical reasoning, numerical simulations and experience, in order that the modelling error remained negligible with respect to the globally required accuracy.

Assuming that the model error is negligible, an estimation procedure was developed, which allowed the number of degrees of freedom of the attitude model to be estimated from the available measurement data. The same estimation procedure, again with the assumption that the model error is negligible, computed the covariance matrix of the estimated unknown variables and then of the reconstructed attitude angles.

The goodness of the approximate mathematical model, that is the assumption that the model error was negligible with respect to the estimation error, was assessed on the basis of the measurement data by suitable statistical tests. When the acceptance of the

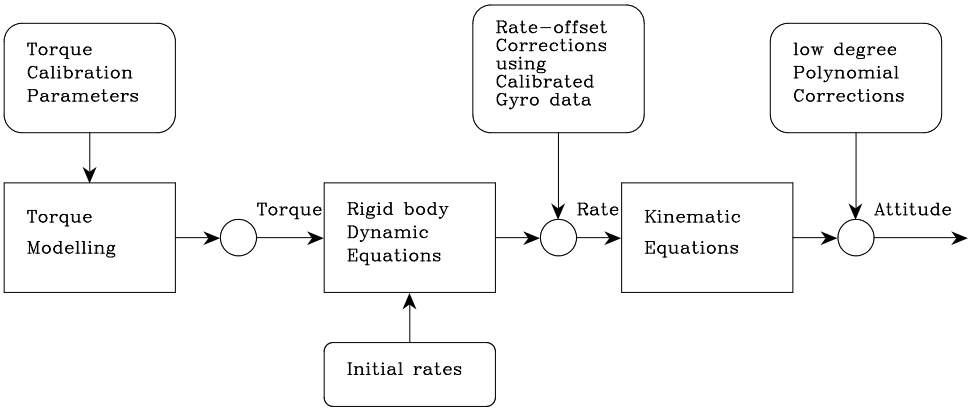

Figure 7.1. *Flow chart of the NDAC attitude determination procedure.*

above hypothesis had too high a risk, the attitude model was adapted by increasing the number of degrees of freedom.

Given the complexity of the problem, involving the estimation of continuous functions of time representing the satellite's response to a wide spectrum of quasi-random perturbations, it is not surprising that the reduction consortia proceeded along very different paths. Briefly, these can be characterised as follows:

The NDAC approach: The dynamical model adopted by NDAC and described in Section 7.2 attempted to represent all the significant torques acting on the satellite (assuming it to be a rigid body), for which the parameters were calibrated as presented in Section 8.5. This approach resulted in a good physical view of why the satellite behaved as it did, and had the great advantage of producing values of the torques which were a great help to ESOC in forecasting the attitude after the passage at the perigee and, even more important, to be the basis of ESOC observing procedures when only two gyroscopes were left. In contrast with FAST, NDAC worked differentially with respect to the nominal scanning law (Section 7.3). The attitude modelling together with the estimation procedure are given in Section 7.4. Figure 7.1 summarises the structure of the NDAC attitude determination procedure.

The FAST approach: The FAST attitude model is given in Section 7.5. It was derived from theoretical considerations supported by accurate numerical simulations based upon dynamical models. It can be noted that, at least between gas jets, this independent approach led to a model very close to the one currently used in astronomy for the rotation of natural bodies. It was proven later, that the whole model is conformable to the classical approach in Celestial Mechanics, even if gas jets occur within the representation interval. Two different models were used: Fourier series and polynomials. They are schematically represented in Figure 7.2.

The main advantage of the NDAC approach was that it permitted the origin of torques to be traced. This allowed ESOC to minimise the time of recovering the attitude after perigee passages. It has also been the basic tool with which it was possible to continue the mission when only two gyroscopes were functioning. The main advantage of the FAST approach was that it could apply to any kind of torque whatever the origin, and this within a very large domain including the recognised torques, with the exception of gas-jet actuation effects for which a specific dynamical treatment was adopted. The second advantage was that no numerical integration was necessary to determine the

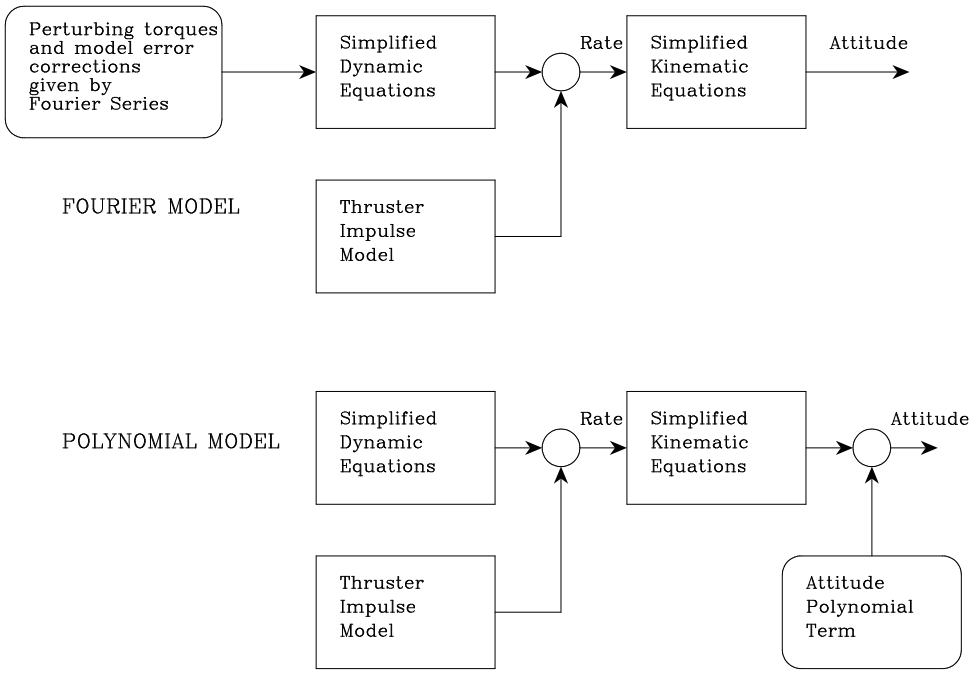

Figure 7.2. *Flow charts of the FAST attitude reconstruction models.*

attitude and the treatment, quite simply, reduced to fitting observations to adequately chosen parameterised expressions.

In conclusion, it is important to stress that both approaches were based on dynamical considerations and that, finally, both converged to numerical descriptions which were assessed as being comparable and well within the margins set by the requirement that the attitude errors should not introduce biases in the reduction on great circles or in Tycho consortium procedures.

7.2. Physics of the Attitude of the Satellite

The satellite attitude describes the positions of the three major axes of the satellite as a function of time. It also describes the rotation rates around these three axes. The positions and rotation rates were affected by a wide range of internal and external torques. The internal torques were caused by the spinning motion of the satellite combined with velocity changes around an axis perpendicular to the main spinning axis. Torques were also caused by an interaction between the rotation axes of the gyros and the spin axis of the satellite, and became particularly noticeable during gyro test runs, when the tested gyro was spun up and spun down. In addition, there were short thruster firing torques. The external torques arose primarily from three sources: solar radiation, gravity gradient and interaction between the magnetic moment of the satellite and the Earth magnetic field. The satellite was also hit a few times by external objects, and was subject to drag, but these occured only at times very close to perigee when observations were not possible anyway. Partial heating of the outer surface during very low perigee passages seems to have played a role too.

Table 7.1. The inertia tensor, in kg m^2, for the Hipparcos satellite. The reference epoch is day 70 in 1991, and t is measured in years from that epoch. The inertia tensor was scaled to a fixed value of I_{xx}.

	x	y	z
x	$534.220 + 0.000t$	$3.459 - 0.469t$	$2.031 + 0.082t$
y	$3.459 - 0.469t$	$590.680 + 0.209t$	$-0.806 + 0.005t$
z	$2.031 + 0.082t$	$-0.806 + 0.005t$	$459.420 - 1.390t$

The motion of the satellite is described by the Euler equation (assuming that the satellite can be considered as a rigid body):

$$\mathbf{I}\,\frac{\mathrm{d}\boldsymbol{\omega}}{\mathrm{d}t} = \mathbf{N} - \boldsymbol{\omega} \times \mathbf{I}\,\boldsymbol{\omega} \qquad [7.1]$$

where $\mathbf{I}$ is the inertia tensor of the satellite, $\mathbf{N}$ the sum of the external torques, and $\boldsymbol{\omega}$ the angular velocity vector. These are all expressed in the satellite reference frame, i.e. with respect to the axes $\mathbf{x}$, $\mathbf{y}$, $\mathbf{z}$ assumed to be fixed in the satellite (Figure 7.3). The (partly calibrated) values for the inertia tensor are given in Table 7.1. Calibration was only possible for the ratios between the diagonal elements and for the relative contributions of the off-diagonal elements. All inertia tensor elements were therefore scaled to a fixed adopted value for I_{xx}, based on the post-launch ground-based estimate for this value (including the effect of the full fuel tank for the apogee boost motor). The calibrations are described in Chapter 8.

The descriptions in the following sections are based on results obtained from the reconstructed attitude as well as theoretical considerations.

Solar Radiation Torques

The solar radiation reflected and absorbed by the outer surface of the satellite caused a force working on the satellite which was not balanced with respect to its centre of mass, and therefore resulted in torques. The size of these torques depended on the orientation of the satellite with respect to the direction to the Sun, and because the satellite had a basic three-fold symmetry, the torques caused by the solar radiation were predominantly a function of 3Ω, where Ω is the angle between the direction to the Sun and the satellite x axis (as in Figure 7.3). The nominal scanning law (see Volume 2, Chapter 8) kept the z axis of the satellite within a 10 arcmin margin from a fixed distance of 43° from the direction to the Sun. The relative position of the x axis, given by the angle Ω, was therefore sufficient to describe these torques.

The periodicity at multiples of 3Ω applied only when the torques were seen in a reference frame fixed with respect to the solar direction. Let $[\,\bar{\mathbf{x}}\ \bar{\mathbf{y}}\ \mathbf{z}\,]$ be such a reference frame with $\mathbf{z}$ along the satellite nominal spin axis, $\bar{\mathbf{x}}$ on the great circle through $\mathbf{z}$ and the direction to the Sun as seen from the satellite, and $\bar{\mathbf{y}} = \mathbf{z} \times \bar{\mathbf{x}}$ completing the triad. The solar radiation torques can be described in this frame as:

$$\bar{\mathbf{N}}_{\mathrm{R}} = \begin{pmatrix} 0 \\ b_0 \\ 0 \end{pmatrix} + \sum_{n=1}^{m} \begin{pmatrix} a_n \sin 3n\Omega \\ b_n \cos 3n\Omega \\ c_n \sin 3n\Omega \end{pmatrix} \qquad [7.2]$$

The torques $\mathbf{N}_R$ as experienced in the satellite reference frame were obtained through a rotation by Ω around the z axis:

$$\mathbf{N}_R = \begin{pmatrix} \cos\Omega & \sin\Omega & 0 \\ -\sin\Omega & \cos\Omega & 0 \\ 0 & 0 & 1 \end{pmatrix} \bar{\mathbf{N}}_R \qquad [7.3]$$

As a result, the solar radiation torques around the satellite x and y axes can be represented as:

$$N_{Rx} = b_0 \sin\Omega + \frac{1}{2}\sum_{n=1}^{m}(a_n - b_n)\sin(3n-1)\Omega + \frac{1}{2}\sum_{n=1}^{m}(a_n + b_n)\sin(3n+1)\Omega \qquad [7.4]$$

and:

$$N_{Ry} = b_0 \cos\Omega + \frac{1}{2}\sum_{n=1}^{m}(b_n - a_n)\cos(3n-1)\Omega + \frac{1}{2}\sum_{n=1}^{m}(a_n + b_n)\cos(3n+1)\Omega \qquad [7.5]$$

This defined the coefficients characteristic for torques caused by the solar radiation.

A further peculiarity of these torques was the fact that their strength varied inversely proportional to the square of the distance between the Earth and the Sun, i.e. by about ±3.5 per cent. The solar radiation torques around the x and y axes were of the order of 2 μNm, which translated into accelerations around these satellite axes at a level of 2.3 mas s^{-2}. Around the z axis the torque and acceleration were about a factor 3 smaller.

The solar radiation torques disappeared during eclipses, and the transitions from sunlit to eclipse were among the most difficult to describe in the attitude reconstruction, in particular as this transition was accompanied by changes in the magnetic moment of the satellite (see below). In addition, during and shortly after a transition, sudden (small) torques occurred, possibly related to the attachments of the solar panels (see also Volume 2, Section 11.4).

Gravity Gradient Torques

The gradient of the Earth's gravitational field across the satellite caused a torque described by:

$$\mathbf{N}_G = \frac{3GE}{r^3}\,\hat{\mathbf{r}} \times \mathbf{I}\,\hat{\mathbf{r}} \qquad [7.6]$$

where $\hat{\mathbf{r}} = \langle \mathbf{r} \rangle$ is the unit length vector indicating the geocentric direction to the satellite's centre of mass, and $r = |\mathbf{r}|$ is the geocentric distance of the satellite (the position vector $\mathbf{r}$ is the same as $\mathbf{g}_0$ in Chapter 12). GE is the geocentric gravitational constant (Table 12.1). $\hat{\mathbf{r}}$ was described in the satellite coordinate system [$\mathbf{x}$ $\mathbf{y}$ $\mathbf{z}$] by means of the two angles ξ_e and Ω_e:

$$\hat{\mathbf{r}} = \begin{pmatrix} \sin\xi_e \cos\Omega_e \\ \sin\xi_e \sin\Omega_e \\ \cos\xi_e \end{pmatrix} \qquad [7.7]$$

These angles were computed from the geocentric ephemeris **r**, given in equatorial coordinates, and the components of the satellite axes, also expressed in the equatorial frame, by means of the relations:

$$\cos \xi_e = \mathbf{z}' \hat{\mathbf{r}} \qquad [7.8]$$

and:

$$\cos \Omega_e = \mathbf{x}' \hat{\mathbf{r}} / \sin \xi_e, \qquad \sin \Omega_e = \mathbf{y}' \hat{\mathbf{r}} / \sin \xi_e \qquad [7.9]$$

Both ξ_e and Ω_e varied with the position of the satellite in its orbit, but near apogee (t_0) the variations in ξ_e were relatively small and Ω_e varied mainly because of the spin of the satellite, $\dot{\Omega}_e \simeq \dot{\Omega}$. Substituting $\Omega_e = \Omega_{e0} + \dot{\Omega} t$ in Equation 7.7 and evaluating Equation 7.6, while considering that the inertia tensor **I** is dominated by the diagonal elements, one finds:

$$\mathbf{N}_{\mathrm{G}} = \frac{3GE}{r^3} \begin{pmatrix} (I_{zz} - I_{yy}) \sin 2\xi_e \sin(\Omega_{e0} + \dot{\Omega} t) \\ (I_{xx} - I_{zz}) \sin 2\xi_e \cos(\Omega_{e0} + \dot{\Omega} t) \\ (I_{yy} - I_{xx}) \sin^2 \xi_e \sin 2(\Omega_{e0} + \dot{\Omega} t) \end{pmatrix} \qquad [7.10]$$

Thus, around apogee the characteristic coefficients for the gravity gradient torque could be recognised by a periodicity with Ω for the x and y axes, and with 2Ω for the z axis, showing a phase shift with respect to the solar radiation torques.

The geostationary transfer orbit in which the satellite was stuck complicated this representation considerably. The amplitude of the torque, ξ_e, and Ω_e became complicated functions of orbital position. This resulted in a signal that was no longer periodic with the rotation period of the satellite, and which was in addition strongly variable in amplitude.

The size of the gravity gradient torque was of the order of 0.2 μNm at apogee, increasing by a factor 200 towards perigee, and dominating the torques from 1.5 hours before to 1.5 hours after the perigee passage.

Magnetic Torques

During the data analysis and the calibrations described in Chapter 8, it was found that the satellite had a distinct magnetic moment of about -2.7 Am^2 directed along the y axis. There also appeared to be a similar size magnetic moment directed along the z axis, existing only during eclipses, when satellite power had switched from solar panels to batteries. The torque caused by the interaction of the magnetic moment vector $\bar{\mathbf{m}}$ and the Earth's geocentric magnetic flux density vector $\bar{\mathbf{B}}$ is given by:

$$\bar{\mathbf{N}}_{\mathrm{M}} = \bar{\mathbf{m}} \times \bar{\mathbf{B}} \qquad [7.11]$$

As seen from the satellite reference frame $\bar{\mathbf{B}}$ is rotating. In the satellite reference frame the flux density vector is expressed as:

$$\mathbf{B} = \begin{pmatrix} \cos \Omega_m & \sin \Omega_m & 0 \\ -\sin \Omega_m & \cos \Omega_m & 0 \\ 0 & 0 & 1 \end{pmatrix} \bar{\mathbf{B}} \qquad [7.12]$$

where Ω_m describes the instantaneous orientation of **B** with respect to the satellite x axis. Within the satellite reference frame **m** was assumed constant. This gave the following relations:

$$\mathbf{N}_{\mathrm{M}} = \begin{pmatrix} m_y B_z - m_z B_y \\ m_z B_x - m_x B_z \\ m_x B_y - m_y B_x \end{pmatrix} \qquad [7.13]$$

Table 7.2. For each of the five gyros, the table gives: (a) orientation of the input axes times the scaling correction factor; (b) the angular momentum (10^{-2} Nms); and (c) the nominally induced torque (μNm).

Gyro		*x*	*y*	*z*
1	*a*	–0.54090	0.89363	–0.00030
	b	1.102	0.675	0
	c	–5.52	9.01	0
2	*a*	0.52620	0.86930	0.00013
	b	0	–1.3	0
	c	10.06	0	0
3	*a*	1.05650	0.00057	–0.00090
	b	0	0	–1.3
	c	0	0	0
4	*a*	–0.00060	0.00080	1.05430
	b	–1.102	0.675	0
	c	–5.52	–9.01	0
5	*a*	0.00154	0.00091	1.05443
	b	–1.102	0.675	0
	c	–5.52	–9.01	0

where at apogee the torques around all three axes were approximately modulated by Ω. Away from apogee this modulation became disturbed due to the changes in $\bar{\mathbf{B}}$, and both the amplitude and the period were varying strongly.

The description for $\bar{\mathbf{B}}$ used the 1985 coefficients of the International Geomagnetic Reference Field (IGRF) (Barraclough 1985), describing the magnetic field as a series of spherical harmonics. The most important (dipole) coefficient is proportional to r^{-3}. The magnetic torques were slightly smaller on average than the gravity gradient torques, but increased in a similar fashion with decreasing distance to the Earth. No corrections were applied for compression or stretching of the field due to interaction with the solar wind. The analysis of the data indicated, however, that such effects were probably present.

Gyro Induced Torques

The five gyros on-board the satellite had 'fixed' spin axes within the satellite reference frame (see Chapter 8). Three of the five gyros were normally active, and each of these would cause a torque on the satellite, depending on the orientation of the spin axis with respect to the satellite spin axis. The orientations of the spin axes and input axes are summarised in Table 7.2. Spinning-up a gyro in addition caused a torque around the spin axis of the gyro. The sum of the torques of the active gyros entered Equation 7.1. The gyros selected for most of the mission were 1, 2, and 4 or 5. The resulting torques from this combination were relatively small.

Thruster Torques

Thruster torques were of very short duration, and intended to change the rotation rates around the satellite axes such as to keep the satellite close to its intended scanning

law. Pulses lasted between 2/75 s and 45/75 s, except close to perigee when longer pulses were permitted. The average $\Delta\omega$ caused by a pulse of one unit of 1/75 s was 0.1 arcsec s^{-1}. The thruster firing strategy changed over the mission, as described in Chapter 8 and in Volume 2, Chapter 13. Thruster firings always took place at the start of an observational frame, and would normally last for no more than 0.25 times the length of a frame. The intervals between firings varied from 200 to 1200 observational frames. Close to perigee the intervals became much shorter. Thruster firings were recorded in the telemetry with the timing and length of the firing for each axis, but information could become ambiguous or get lost due to telemetry problems. Chapter 8 describes the thruster firing calibrations.

Incidental Micrometeoroid Hits

Incidental hits due to micrometeoroids (see Volume 2, Chapter 6) had the same appearance as thruster firings, except that they were evidently not recorded in the telemetry and not tuned to the start of an observational frame. Two fairly serious hits and many minor hits were detected from examinations of the gyro read outs. They were also conspicuous in the course of the great-circle reductions (see Chapter 9).

Miscellaneous Effects

A torque possibly related to thermal radiation from the satellite after perigee passages was noted in the examinations of the accelerations of the satellite (see Chapter 8, Figure 8.16). Depending on the height of perigee, which varied between 440 and 580 km above the Earth surface, the satellite was more or less affected by drag. As the rotation period of the satellite was relatively long with respect to the time the satellite was exposed to drag, this affected the satellite in an unbalanced way. After perigee, the satellite had been warmed up on one side and started losing this excess heat through radiation, which due to its distribution over the surface, could cause a small torque. The size of this effect was at most of the order of 0.02 μNm.

7.3. The Nominal Scanning Law and Real-Time Attitude Determination

The scanning of the sky by the satellite proceeded along a pre-determined nominal scanning law. This scanning law had been designed such as to optimise the coverage of the sky, while avoiding the sunlight to affect the measurements. As this was a scanning satellite, this meant that scanning circles always had to be inclined with respect to the ecliptic plane. The scanning law is for this reason described in the ecliptic coordinate system. The details of the scanning law can be found in Volume 2, Chapter 8. Here the importance is in the relation between the equatorial coordinates and the satellite's main axes. These relations are described by a series of orthogonal rotations. If we denote by $\mathbf{R}_i(\alpha)$ the rotation of a coordinate triad around axis i by an angle α, then for the transformation from equatorial direction cosines $\mathbf{e}$ to satellite coordinates $\mathbf{s}$ the following relation applies:

$$\mathbf{s} = \mathbf{R}_3(-\Omega)\mathbf{R}_2(\xi - \frac{\pi}{2})\mathbf{R}_1(\frac{\pi}{2} - \nu)\mathbf{R}_3(-\lambda_\odot)\mathbf{R}_1(-\epsilon)\mathbf{e} \qquad [7.14]$$

where ϵ is the inclination of the ecliptic plane for equinox J2000.0, and $\lambda_\odot$, ν, ξ and Ω are the angles in which the nominal scanning law was described. They were referred to

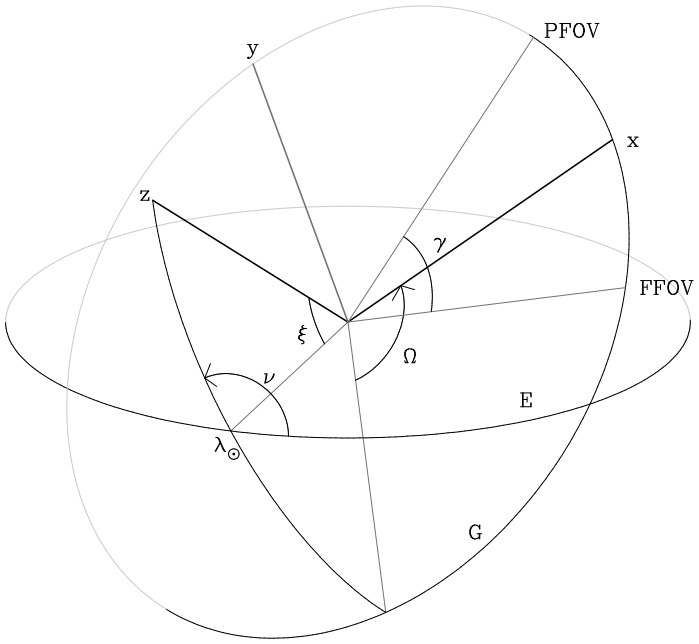

Figure 7.3. *The heliotropic angles ($\lambda_\odot$, ν, ξ, Ω) and the satellite axes (**x**, **y**, **z**) in the ecliptic reference frame. The ecliptic is indicated by 'E', the scanning circle by 'G'. The two fields of view (PFOV, FFOV) and the basic angle γ are also indicated.*

as the 'heliotropic angles' and are shown in Figure 7.3. Of these, all but ξ were time dependent.

The inertial rates resulting from the nominal scanning law were accordingly given by:

$$\boldsymbol{\omega}_n = \begin{pmatrix} -\cos\xi\sin\nu\cos\Omega - \cos\nu\sin\Omega & \sin\xi\cos\Omega & -\sin\Omega & 0 \\ \cos\xi\sin\nu\sin\Omega - \cos\nu\cos\Omega & -\sin\xi\sin\Omega & -\cos\Omega & 0 \\ \sin\xi\sin\nu & \cos\xi & 0 & 1 \end{pmatrix} \begin{pmatrix} \dot{\lambda}_\odot \\ \dot{\nu} \\ \dot{\xi} \\ \dot{\Omega} \end{pmatrix} \qquad [7.15]$$

where in this case $\dot{\xi} = 0$.

The real-time attitude determination was provided in the form of three small rotation (Tait-Bryan) angles relative to the nominal attitude. These Tait-Bryan angles could be added to the nominal attitude heliotropic angles to provide a new set of heliotropic angles, giving the actual rather than the nominal satellite attitude. The Tait-Bryan angles were given by Θ_1, Θ_2 and Θ_3. The following quantities are defined:

$$\begin{aligned} A &= \cos\Omega\sin\Theta_1\cos\Theta_2 - \sin\Omega\sin\Theta_2 \\ B &= (\cos\Omega\cos\Theta_2 - \sin\Omega\sin\Theta_1\sin\Theta_2)\sin\xi - \cos\xi\cos\Theta_1\sin\Theta_2 \\ C &= \sin\xi\sin\Omega\cos\Theta_1 - \cos\xi\sin\Theta_1 \\ D &= (B^2 + C^2)^{1/2} \end{aligned} \qquad [7.16]$$

These define the new heliotropic angles as:

$$\begin{aligned} \hat{\lambda}_{\odot} &= \lambda_{\odot} \\ \hat{\xi} &= \arcsin D \\ \hat{\nu} &= \nu + \arcsin(A/D) \\ \hat{\Omega} &= \Omega + \Theta_3 + \arcsin C \end{aligned} \qquad [7.17]$$

The real-time attitude determination operated on-board the satellite and provided a record of the satellite in Tait-Bryan angles. The process of updating the Tait-Bryan angles was based on a mixture of gyro data and star mapper transit times. The gyro data were transformed to inertial rates, then corrected for the inertial rates resulting from the nominal scanning law and then transformed into corrections to the Tait-Bryan angles. Correctly recorded star mapper transits were used to control and correct the resulting Tait-Bryan angles. The rate estimates supplied as part of the real-time attitude determination were based on the evolution of the Tait-Bryan angles and could be badly affected by a sudden change in these angles, such as caused by an update from the ground. These updates were required to assist the satellite in recovering attitude convergence after long gaps in the observations, in particular after a perigee passage.

7.4. Attitude Modelling and Estimation by NDAC

By integrating numerically the Euler equation, using the full representation of the inertia tensor and the most accurate approximations of the torques, an accurate description was obtained of the rates of the satellite. These rates would normally include an offset caused by an error in the starting point. This error was largely removed by adjusting the rates to the observed gyro rates through linear offsets. The rates could then be integrated to provide a first approximation to the actual attitude angles. This integration was also affected by an error in the starting point, as well as by minor errors in the original model. These last adjustments were corrected using star mapper transit data. By calibrating the thruster firing performance, it was possible to carry the integrations across the thruster-firing discontinuities in the velocities and acceleration. This was basically the method adopted by NDAC.

The *a priori* detection of any discontinuities in the rotation rates was very important. Most discontinuities were known: they were due to thruster firings, for which information was stored in the telemetry. Some discontinuities were, however, not recorded in the telemetry. In order to find these, the gyro rates were examined for every data set for the coincidence of thruster firings and rate discontinuities. Through these examinations thruster firings were detected for which information was lost due to telemetry problems, as well as sudden rate changes due to the satellite being hit by a micrometeoroid. Also the start and end time of gyro spin-up and spin-down events were recognised. All such events were entered into the data stream as pseudo thruster firings. The attitude solution would not cross these events but instead provide solutions up to, and starting from these instances.

The calibrations used in the NDAC attitude reconstruction made it necessary to repeat the process two to three times: the reconstructed data was used to improve the calibration results which were subsequently reused in the reconstruction. At the same time, improved reference positions for the star mapper stars were introduced. A schematic flow chart of the NDAC attitude determination procedure is given in Figure 7.1.

Integration of the Torques to Inertial Rates

The first step in the NDAC attitude reconstruction consisted of estimating, by integrating the Euler equation (Equation 7.1), the rotation rates around the three satellite axes, over intervals between thruster firings. The torques were obtained from calibrations using earlier reconstructed attitude results. This integration needed as a starting point a relatively accurate estimate of the rotation rates at the start of the interval, which was, for the first interval considered, obtained from gyro data. For subsequent intervals it was obtained by integrating across thruster firings (see below). In normal mode (no thruster firings), the accelerations were calculated in time steps of 0.71 s (at reference times −1.066 s, −0.355 s, +0.355 s with respect to the centre of an observational frame of 2.133 s). The accelerations were numerically added to the rotation rates (at reference times −0.71 s, 0.0 s, +0.71 s). All three rotation rate estimates per observational frame were stored. Experiments with shorter integration times showed that for normal conditions the time step used was sufficiently small.

The time step for the integration of the Euler equation was set by the rate of change of the cross product $\boldsymbol{\omega} \times \mathbf{I}\boldsymbol{\omega}$ in Equation 7.1. This was partly accommodated by provisionally extrapolating $\boldsymbol{\omega}$ to the central time of the integration interval. The rate of change of $\boldsymbol{\omega}$ was within a range of ±3 mas s^{-2}, which gave a change in the accelerations, resulting from the cross product, of the order of 2.5×10^{-4} mas s^{-3}. The uncertainty in the accelerations resulting from the estimates of the external torques was approximately 10 times larger. Using time steps of 0.71 s the error on the velocities obtained from the integration generally accumulated to no more than about 1 to 2 arcsec s^{-1} over a time interval between thruster firings (ranging from 300 to 2000 s), except for cases where the initial rate estimates at the start of the integration had been very uncertain due to excessive gyro noise or telemetry problems. Due to uncertainty of the reconstructed external torques, decreasing the time steps would have increased precision without improving accuracy.

Integrations were carried out in this manner until a thruster firing or an interruption was encountered, at which point the first inertial rate estimates $\boldsymbol{\omega}_t$ over an interval had been obtained, described by three estimates per observational frame.

The rates $\boldsymbol{\omega}_t$ obtained from the torque integration were adjusted to the observed (and calibrated) gyro rates by applying an offset and a linear correction with time. When available, the rate around the z axis was also fitted with scanning rates derived from the great-circle reduction. The gyro data were corrected for drift and orientation (see Chapter 8) and weighted according to the specific gyro noise levels. As gyros were recording rotation rates coming from all three axes, one solution was made for the three axes together. Thus, the equations solved by the method of least-squares were:

$$\mathbf{a} + (t - t_0)\mathbf{b} = \mathbf{T}(\mathbf{g} - \mathbf{g}_0) - \boldsymbol{\omega}_t + \boldsymbol{\epsilon}_g \qquad [7.18]$$

where $\mathbf{g}$ represents the gyro observations, which were corrected for drift ($\mathbf{g}_0$) and transformed to rotation rates around the three satellite axes through matrix $\mathbf{T}$, obtained from Table 7.2. The time t was measured in units of 100 s relative to a reference time t_0 halfway into the thruster firing interval. The errors on the gyro readings were given by $\boldsymbol{\epsilon}_g$, for which the variances were known from the gyro calibration process described in Chapter 8. These variances had been determined over an entire data set (6 to 8 hours of observations), and compared for consistency with neighbouring data sets. The square-root variances for the gyro data ranged from 0.008 arcsec s^{-1} to 0.1 arcsec s^{-1}. With

the errors at the low end of the range the gyro data were contributing to the attitude solution, while with errors at the high end of the range, the contribution was effectively restricted to providing estimates of the star mapper scan velocities (see also Section 8.3).

The variance observed over an interval between thruster firings was used as an indication for the data being sufficiently well described by Equation 7.18. There was also the possibility of rejecting outliers in the gyro data, but this was rare under normal conditions, and had to be suppressed under bad conditions (noise bursts). When the variance observed over an interval was higher than expected, the gyro data were examined for discontinuities. Many such cases revealed instances when the satellite had been hit by a micrometeoroid, causing (mostly small) discontinuities in the rotation rates. At such discontinuities, an artificial thruster firing event was added to the data set to account for the discontinuity, which then split the solution over the interval investigated into two separate intervals.

The solution of Equation 7.18 led to $\boldsymbol{\omega}_g = \boldsymbol{\omega}_t + \mathbf{a} + (t - t_0)\mathbf{b}$, the estimated inertial rates based on the integrated torques and gyro data. These rates were used in the star mapper reductions (see Chapter 6) for the determination of the effective slit spacings. Using $\boldsymbol{\omega}_g$, an estimate of the rotation rates at the end of the thruster-firing interval was obtained, providing the rates at the start of the next thruster firing.

The integration of Equation 7.1 was carried across the thruster firing using information obtained from the thruster calibrations. Here, however, the time step was much shorter in order to accommodate the very rapidly changing rotation rates. Every 0.71 s interval used in the normal integration was subdivided into 160 intervals of 1/225 s, still providing the three estimates of the rotation rates per observational frame. The 'cross-talk' effect of the thrusters (described in Chapter 8 and primarily resulting from the shift in the position of the centre of mass due to the full apogee boost motor tank), was fully taken into account, as were the 'zero points'. Thus, a firing on the z axis would also cause small velocity changes for the x and y axes rotations. At the end of a thruster firing integration, estimates of the rotation rates for the start of the next thruster firing interval had been obtained.

The solutions for Equation 7.18 over all intervals contained in a uninterrupted stream of data (interruptions could be due to gaps in the data containing one or more thruster firings, or so-called pseudo thruster firings, representing various discontinuities in the rotation rates) were all connected through conditions describing the expected changes in the rotation rates across thruster firings relative to the corrections already applied. The final solutions for Equation 7.18 were obtained from such a chain of simultaneously solved, linked least-squares solutions, and applied to the estimates $\boldsymbol{\omega}_t$.

Integration of the Rates

Given an estimated *a priori* orientation of the satellite axes, the inertial rates could be used to evaluate those orientations as a function of time, providing the first estimate of the satellite attitude. The attitude at this stage was described with respect to the nominal attitude in the form of Tait-Bryan angles. This allowed some incorporation of data from the real-time attitude determination, which was described in the same way. If the satellite were to follow exactly the nominal scanning law, then this would result in inertial rotation rates given by $\boldsymbol{\omega}_n$ (as described in Section 7.3, Equation 7.15). These rates were, however, described in a slightly different coordinate system: the coordinates of the nominal scanning law, with respect to which the satellite was displaced by the

Tait-Bryan angles. Thus, in order to evaluate the evolution of the Tait-Bryan angles relative to the nominal attitude, the difference $\delta\boldsymbol{\omega} = \boldsymbol{\omega}_g - \mathbf{R}\boldsymbol{\omega}_n$ had to be integrated, where $\mathbf{R} = \mathbf{R}_3(\Theta_3)\mathbf{R}_2(\Theta_2)\mathbf{R}_1(\Theta_1)$. The integration to position angles needed a starting point. At the start of an interval, a real-time attitude determination position was used as such. However, the real-time attitude determination was not always converged at such a point. This was shown in the data from the examination of the star mapper reduction results (see below). In such a case the interval was rejected, and the integration started again for the next interval, until the attitude appeared to have converged. From then on the integration could proceed unaided by real-time attitude determination data.

The transformation from $\delta\boldsymbol{\omega}$ to increments of the Tait-Bryan angles $\boldsymbol{\Theta}$ were obtained from:

$$\frac{\mathrm{d}\boldsymbol{\Theta}}{\mathrm{d}t} = \begin{pmatrix} \cos\Theta_3 / \cos\Theta_2 & -\sin\Theta_3 / \cos\Theta_2 & 0 \\ \sin\Theta_3 & \cos\Theta_3 & 0 \\ -\cos\Theta_3 \tan\Theta_2 & \sin\Theta_3 \tan\Theta_2 & 1 \end{pmatrix} \delta\boldsymbol{\omega} \qquad [7.19]$$

where the time step dt was 1/22.5 s for normal observational frames (2.133 s), and 1/225 s for the first half of an observational frame starting with a thruster firing (thruster firings never lasted for more than half an observational frame, and mostly did not last for more than 0.5 s). In the numerical integration $\delta\boldsymbol{\omega}$ was calculated for the central time of the integration interval, using the three estimates of $\boldsymbol{\omega}_g$ per observational frame in the form of a second order polynomial describing the estimated inertial rates at any time during the frame. For frames with thruster firings the estimates of the rates also used the lengths of the firings on each axis. Experiments with time steps of different lengths had shown that there was no significant loss of accuracy for the time steps used (the numerical accuracy over a thruster firing interval was much higher than the expected accuracy of the attitude angles).

In the first solution of the attitude, when star mapper transit times were still to be determined, the estimated Tait-Bryan angles were fitted to the real-time attitude determination Tait-Bryan angles, providing a kind of smoothed and stabilised real-time attitude estimate. These fits were done with only an offset or at most a linear time dependence in order to preserve the dynamical model. Such a fit was only needed in order to produce predicted star mapper transit times, which could be compared with observed transit times. The comparison, which was preserved in the form of a graph for data in every orbit, showed the convergence of the real-time attitude determination in both fields of view as a function of time. This allowed the detection and early elimination of bad convergence time intervals from the data (see Figure 6.3).

The results of the integration were stored in the form of heliotropic angles (see Equations 7.16 and 17), at the three reference times per frame that were earlier used for the inertial rates (see above).

Final Attitude Corrections

The preliminary attitude angles obtained this way were used together with star mapper transit times to determine the actual satellite attitude angles. The three estimates per observational frame of the heliotropic angles were represented through second order polynomials, describing the angles and their rates of change at the exact time of the transit. When star mapper transit times still had to be calculated, the rates of change of the heliotropic angles were translated into inertial rates around the satellite axes, using Equation 7.15, and subsequently into inertial rates along the scan direction and perpendicular to the scan direction for each field of view. These rates were then used

in the determination of star mapper transit times (see Chapter 6), and the heliotropic angles were recalculated for the observed transit time.

The heliotropic angles and the apparent stellar coordinates, were used to calculate the predicted coordinates (η, ζ) in the field of view. These coordinates were related to the expected coordinates, defined by the star mapper geometry. The differences between the observed and predicted value for η, $\delta\eta$, were expressed in three coordinates: a correction to the scan phase ($\delta\psi$), and corrections to the attitude angles perpendicular to the scan-direction in the preceding ($\delta\theta_p$) and following field of view ($\delta\theta_f$):

$$\delta\psi + g\,\delta\theta_{p,f} + \epsilon_\eta = \delta\eta \qquad [7.20]$$

Here $g = 0$ for the vertical slit group and ± 1 for the inclined slit group of the upper and lower branch respectively, and suffix p or f applies according to the field of view of the transit. The variance of the error on the transit time, ϵ_η, was known from the star mapper processing.

The corrections $\delta\psi$, $\delta\theta_p$ and $\delta\theta_f$ were expressed as polynomials in time, with the order depending on the length of the interval, the amount of data available, and the demands placed by the observations. The polynomial degree was always initialised at a minimum level (usually 1 or 2), and increased when the observed variance indicated that the solution was inadequate, up to a point where it was considered that insufficient data was available for any further increments. The need for increments was determined on the basis of the observed unit weight variance. Although one solution was made for the three coordinates together, variances were calculated for each coordinate separately, and also increments of polynomial degree were decided independently. Preliminary solutions were made over intervals between thruster firings. Boundary conditions were imposed that linked these solutions across the thruster firings. These boundary conditions forced approximate, and not exact, continuity of the solutions across thruster firings, thus accommodating the uncertainties imposed by the thruster firing calibrations. The final solution was made over all intervals and boundary conditions without further iterations.

The estimation standard errors on the reconstructed attitude were calculated from the local (thruster firing interval) normal equations matrix, $\mathbf{A}$, of the fitted attitude parameters through a convolution with the basis functions at the centre of every observational frame. These estimated errors agreed also with the requirements of the Tycho data reductions, which used the NDAC reconstructed attitude results. Thus, if $\mathbf{f}(t)$ was the vector of basis functions for one of the attitude angles in the interval considered, and the unit weight error of the solution was u, then the uncertainty in the attitude angle was given, as a function of time, by:

$$\sigma(t) = u\,\left[\mathbf{f}(t)'\mathbf{A}^{-1}\mathbf{f}(t)\right]^{1/2} \qquad [7.21]$$

When the uncertainty was above 0.3 arcsec the data was flagged as ‘bad’. In the error evaluation, only this last solution was relevant: all preceding steps provided the smooth background relative to which the final solution was made.

The final transformation from $\delta\psi$, $\delta\theta_p$ and $\delta\theta_f$ to corrections of the heliotropic angles was given by:

$$\begin{aligned}
\widetilde{\lambda}_\odot &= \hat{\lambda}_\odot \\
\tilde{\xi} &= \hat{\xi} + (\delta\phi \sin\Omega - \delta\theta \cos\Omega) \\
\tilde{\nu} &= \hat{\nu} - (\delta\phi \cos\Omega + \delta\theta \sin\Omega)/\sin\xi \\
\widetilde{\Omega} &= \hat{\Omega} + \delta\psi + (\delta\phi \cos\Omega + \delta\theta \sin\Omega)\tan\xi
\end{aligned} \qquad [7.22]$$

where $\delta\phi = (\delta\theta_p - \delta\theta_f)/2\sin(\gamma/2)$, $\delta\theta = (\delta\theta_p + \delta\theta_f)/2\cos(\gamma/2)$ and γ is the basic angle between the fields of view. The incremental angles $\delta\psi$, $\delta\theta$ and $\delta\phi$ were approximately the same as those used in the attitude reconstruction by FAST.

In conclusion, the NDAC attitude was determined by using star mapper transit data to determine small corrections relative to a dynamical model for the satellite, which was supplemented with gyro observations.

Basic Angle and Star Mapper Geometry Calibration

Three components of the star mapper geometry were calibrated using the attitude reconstruction processes: the orientation of the slits with respect to the scanning circle (defined as the great circle going through the intersecting points of inclined slits in the preceding and following fields of view), the separation between the vertical and inclined slits and the basic angle between the two fields of view for the vertical slits (due to projection and distortion effects this was slightly different from the basic angle for the main grid). These calibrations were carried out using star mapper transit time residuals obtained from the attitude reconstruction solution, accumulated over 2 to 3 days. The residuals were accumulated in histograms (68 bins) as a function of vertical coordinate H of the transit. Each bin coincided with a scan-field, the basic element used in manufacturing the grid. Medians in each bin were fitted with an offset and a linear function of the H coordinate. These fits were made for the two slit groups and the two fields of view separately. The offsets measured were of the order of 10 to 30 mas, representing small basic-angle corrections and corrections for the slit-group separation. The rotations (relative to the main 5 arcmin rotation) were of the order of 0.3 to 0.7 arcsec.

The remaining residuals were accumulated in a histogram to provide the medium-scale distortion corrections. These corrections were of the order of 0.1 arcsec or less, and were further improved in the Tycho data reduction (see Volume 4, Section 7.3). The final correction, describing the position of the star mapper slits with respect to the main grid reference line, was provided by the great-circle reduction, presented in Chapter 9.

7.5. FAST Attitude Model

Assuming an attitude model with a finite number of degrees of freedom, the model error is defined as the difference between the true attitude and the attitude that could be reconstructed by using in an optimal way the degrees of freedom of the model if measurement data without any error were available. Then, according to an attitude estimation method, which was based on this model, the estimation error is defined to be the effect on the attitude reconstruction of the actual measurement errors, if the models were perfectly correct.

The model error can be evaluated by simulations assuming the true system is perfectly known, however it cannot be evaluated by experimental data corrupted by measurement errors. In this latter case the model error can be monitored by significance tests, which, assuming by hypothesis that the model is correct, gives the *a priori* probability of getting the resulting test values. When this probability is too low the hypothesis tested is usually rejected. On the other hand, the estimation error caused by the measurement errors

can be evaluated by the estimation procedure, assuming, of course, that the model error is negligible.

For these reasons it was required that the model error should be negligible with respect to the estimation error, setting its maximum limit, evaluated by simulations, to the order of several mas. It is generally possible to reduce the model error by increasing its number of degrees of freedom, but, of course, the estimation error increases with the number of degrees of freedom. The research was oriented to get the required model accuracy with the smallest possible number of degrees of freedom.

The use of the rigid body equations to describe the satellite motion was excluded because it was considered that it was too difficult to calibrate, with the required accuracy, the telescope reference frame position with respect to the inertial axes of the satellite, and to maintain such an accuracy throughout the mission. Similarly the use of torque models derived from physics was excluded because at the level of the required accuracy they would require too large a number of degrees of freedom, and above all because it is never possible to be sure that all the non-negligible causes have been taken into account. This method was nevertheless successfully implemented by NDAC (see previous section).

Particular attention was devoted to the choice of the attitude angles. In fact, the various sets of three angles are related among themselves by non-linear transformations so that their choice influences the simplicity of the attitude model, the estimation method, and accuracy.

FAST Attitude Angles

The FAST attitude representation was described relative to the reference great-circle frame (Section 11.2), defined by the position of its pole in ecliptic coordinates, λ_R and β_R. This pole was selected as the position of the z axis in the nominal scanning law for a reference time halfway between the start and the end of the data set concerned. Relative to this reference system, three attitude angles were defined: ψ, θ and ϕ. They are related to the classical 3-2-1 Euler angles ψ_e, θ_e and ϕ_e by:

$$\phi = \phi_e, \qquad \theta = \theta_e, \qquad \psi = \psi_e - \arctan\left(\frac{\sin\theta \sin\phi}{\cos\theta + \cos\phi}\right) \qquad [7.23]$$

The choice of the angle ψ was motivated by the fact that it models the scanning motion better, because its rate of change is much closer to the rotation rate around the satellite z axis. It was in addition proven that estimation results obtained with these angles were significantly better than those obtained by keeping ψ_e.

Approximate Motion Equations

The ϕ, θ, ψ attitude angles are modelled as the outputs of the following two independent systems of differential equations, which were obtained as an approximation of the satellite dynamic equations in the case of small perturbations:

$$\begin{aligned} \dot{\omega}_z &= \delta_z(t) \\ \dot{\psi} &= \omega_z \end{aligned} \qquad [7.24]$$

and:

$$\begin{aligned} \dot{\omega}_x &= \delta_x(t) \\ \dot{\omega}_y &= \delta_y(t) \\ \dot{\phi} &= -\omega_0\theta + \omega_x \\ \dot{\theta} &= \omega_0\phi + \omega_y \end{aligned} \qquad [7.25]$$

where ω_0 is a constant parameter equal to the nominal spin rate.

The functions $\delta_x(t)$, $\delta_y(t)$, $\delta_z(t)$ are the derivatives of the rate components ω_x, ω_y, ω_z. In a first rough approximation they model the effect of the torque acting on the satellite, but more precisely they have been introduced not only to model the torque effect but also to compensate for the approximation introduced by using the above simplified equations to model the telescope motion. It is well known that any given set of three continuous time functions $\phi(t)$, $\theta(t)$, $\psi(t)$ can be obtained as the output of the above dynamic system by the application of a suitable set of input functions $\delta_x(t)$, $\delta_y(t)$, $\delta_z(t)$ and by initial conditions. Then, in principle, the model error can be reduced as much as required by attributing a sufficient number of degrees of freedom to the input functions.

System Input Functions

The system inputs $\delta_{x,y,z}(t)$ are decomposed into the sum of two terms, respectively the control inputs $u_{x,y,z}(t)$ and the disturbances $d_{x,y,z}(t)$. The control inputs are introduced to describe the effects of the on-board attitude control: they are assumed to be a sequence of ideal pulses (Dirac functions) of unknown amplitude applied at the central time of the gas-jet actuations. The disturbances are introduced to describe the effects produced by the perturbing torques and to keep into account, at the same time, the difference between the above simplified dynamic system and the reality. The disturbances are expressed by different mathematical models (Fourier and polynomial models) depending on the length of the time interval considered and the satellite perturbing conditions. In the case of Fourier models the disturbances are described by a Fourier series with unknown coefficients and the response of the system is computed on the basis of the above differential equations. In the case of polynomial models the system forced response to the disturbances is directly described by polynomial series. The resulting attitude model is presented in the two cases in Figure 7.2. The following models were used:

- long-term Fourier model: this was the standard model, used in normal operating conditions over a time interval corresponding to a full rotation around the satellite z axis, i.e. 128 min. Independently from the actual duration of the considered time interval, the disturbances are described by a Fourier series whose fundamental harmonics have the frequency ω_0 corresponding to the satellite nominal spinning rate used in the approximate equation of motion (Equation 7.25). In this case the forced solution of the differential equations has the form:

$$\begin{aligned} \phi_d(t) &= b_{s0}t\sin\omega_0 t + b_{c0}t\cos\omega_0 t + \sum_{k=2}^{n}[b_{sk}\sin(k\omega_0 t) + b_{ck}\cos(k\omega_0 t)] \\ \theta_d(t) &= c_{s0}t\sin\omega_0 t + c_{c0}t\cos\omega_0 t + \sum_{k=2}^{n}[c_{sk}\sin(k\omega_0 t) + c_{ck}\cos(k\omega_0 t)] \\ \psi_d(t) &= \sum_{k=1}^{m}[a_{sk}\sin(k\omega_0 t) + a_{ck}\cos(k\omega_0 t)] \end{aligned} \qquad [7.26]$$

A different number of harmonics in the range 12 to 36 was used in modelling ψ (m) and in modelling θ and ϕ (n). The number of harmonics was determined by an adaptive method based on the computation of the Fisher-Snedecor test (Cramér, 1946). The adaptation was made by increasing the number of harmonics by 3 at a time, starting from 12. The optimal number was the maximum number for which the Fisher-Snedecor test value was still above a given threshold;

- intermediate term Fourier model: this model was used over intervals of 30 min to 115 min. The perturbing torques were modelled as above by a finite Fourier series of unknown amplitude harmonics (Equation 7.26), but without the mixed terms for ϕ and θ (describing the torque caused on ϕ through the change of θ and *vice versa*). Here the fundamental period was chosen equal to the length of the time interval, and the minimum number of harmonics at the start of the computation was determined by the interval length. They were increased by one at a time, followed by the tests described above, until a test value within a given threshold was obtained;
- short-term polynomial model: this model was used for the shortest considered time intervals, namely a period between two thruster firings (varying from a few minutes to more than half an hour, but on average about 12 to 15 minutes). The perturbing torque effect was modelled by Legendre polynomials, the degree of which was adapted to the considered case, independently for ψ and for θ and ϕ. The polynomial degrees were increased by one at a time until the Fisher-Snedecor test value obtained was within a given threshold;
- short-term polynomial model in penumbra: while the satellite was in penumbra, before and after an eclipse, the solar radiation torque followed a transient from high values to very low or *vice versa*. Conditions during different transients were similar but never the same. The transient was modelled as a stochastic process for which a Karhunen-Loève expansion (Papoulis 1991) was computed. This provided an ordered set of orthonormal functions, of which each one was approximated by a Legendre polynomial representation. The first 10 (ψ) and 15 (θ and ϕ) functions were stored. The order of the Karhunen-Loève expansion used was adapted to the particular case considered, starting from a minimum value determined by the number of star mapper transits available, up to the maximum number of stored functions, applying at each step the Fisher-Snedecor test.

7.6. FAST Estimation Procedure

The Different Attitude Estimation Algorithms

The uncertainty with which the attitude can be determined depends upon the precision with which star positions are known. Since the positions provided by the Input Catalogue had not the required accuracies, an iterative procedure was adopted by FAST for the Hipparcos data reduction based upon successive improvements of star positions which, in turn, were used to improve the attitude (see Chapter 4). This required the implementation of three different attitude reconstruction algorithms.

First year attitude reconstruction (OGARO): Input Catalogue errors were taken into account modelled as uncorrelated random variables with known variance. The star coordinates were estimated together with the attitude angles.

Standard attitude reconstruction (OGAR): After the first Hipparcos catalogue construction, the errors affecting the apparent coordinates, whether they were improved or not, were no longer considered as unknowns. An equivalent standard deviation of the transit time was introduced which was obtained by the combination of errors in the star mapper transit time measurements, the star mapper calibrations, and the star coordinates. The software estimated the attitude angles only, assuming that the apparent star coordinates were perfectly known.

Iterated attitude reconstruction (OGARI): The satellite rotation around the z axis obtained by the great-circle reduction was used as additional input data, together with the star mapper transit times. This mode was used for the final iterations of the catalogue.

These estimation algorithms are not significantly different from the point of view of their methodology. They will be illustrated as applied to OGAR.

Principle of Attitude Estimation

The only types of data used for the attitude reconstruction were the star mapper transit times and apparent star coordinates, with their respective standard deviations, and the central time instants of thruster firings. Gyro measurements and real-time attitude data were not used, as these data were not found to be accurate enough to give a useful contribution to the attitude reconstruction accuracy both because of the gyro measurement errors and the errors of the position of their axes in the telescope frame.

Assuming the attitude model given in Section 7.5 and the availability of the above measurement data, a measurement equation was written for each star transit obtained by star mapper data processing (Chapter 6). Such equations require that the measured transit time is equal to the sum of an ideal transit time, expressed by a function of the attitude angles, star coordinates and calibrated star mapper geometry, and of the errors resulting from the star mapper data processing, the star catalogue used and the star mapper calibrations.

The attitude model was then inserted into the measurement equations, yielding a set of equations where the unknown variables were given by the degrees of freedom of the attitude model. The data was divided in time segments, always starting and ending with thruster actuations. The attitude was reconstructed for each segment in one step through the solution of a set of simultaneous equations, using the maximum likelihood estimation criterion to determine the unknown parameters by maximization of the measurement error probability. A Gaussian distribution of the errors was assumed and the solution was obtained working at a second-order level with the Gauss-Markov method. The unknown parameters of the attitude model and their covariance matrix were estimated and used to calculate the attitude angles and their standard deviations.

The rest of this section gives a more detailed account of the processes outlined above.

Measurement Equation and Estimation Procedure

For each detected star mapper transit the following data were available:

- the transit time $\hat{\tau}$ and its standard error as evaluated in the star mapper data processing. Using the instantaneous rotation rate, the standard error could be expressed as an error angle ϵ;
- the apparent stellar coordinates (v, r) in the reference great-circle frame, with their standard deviations whenever they came from the Input Catalogue and were not improved by an intermediate sphere solution;
- the field of view index ($f = +1$ for preceding and $f = -1$ for following) and the slit-group index ($g = 0$ for vertical, $g = +1$ for upper inclined, $g = -1$ for lower inclined);
- the reference position of the slit group, $\eta_0(f,g)$. This position consists of $f\gamma/2$ (where γ is the basic angle) and the distance between the fiducial reference line for the main grid and the reference line for the slit group (G_v or G_i in Section 6.1);
- the calibrated grid-to-field transformation for the star mapper with its standard deviations (see Chapter 6).

On the basis of the above data the following measurement equations were written for a vertical slit transit:

$$\psi = v + \eta_0(f,g) + \Delta\eta_{fg}(\phi,\theta,r) + \epsilon_v \qquad [7.27]$$

and for a transit through the inclined slits:

$$-\phi f g \sin\eta_0 - \theta g \cos\eta_0 = v + \eta_0(f,g) - gr - \Delta\eta_{fg}(\phi,\theta,r) - \psi + \epsilon_i \qquad [7.28]$$

where the attitude angles refer to the observed transit time $\hat{\tau}$. ϵ_v and ϵ_i are random variables due to the errors in transit time estimate, apparent star coordinates, and the star mapper calibration. Their standard deviations were calculated from the input data. $\Delta\eta_{fg}$ are complicated non-linear functions of ϕ, θ, r including corrections from the calibrations. The terms $\Delta\eta_{fg}$ have small derivatives with respect to the variables ϕ, θ, r in all their admissible range. This particular property allowed these equations to be considered as linear in the variables ϕ and θ, and to be updated in an iterative procedure.

When a time interval and an attitude model had been selected the attitude angles $\phi(t)$, $\theta(t)$, $\psi(t)$ were computed as functions of the degrees of freedom of the model by solving the differential equation system, Equations 7.24 and 7.25. Since the system is linear, the attitude angles were obtained from the linear measurement Equations 7.27 and 7.28, and a set of equations was obtained in the unknown variables corresponding to the degrees of freedom of the model. As already pointed out, $\Delta\eta_{fg}$ could be computed from tentative values of ϕ and θ, so that the above system of equations could be assumed linear in the unknown variables.

The unknown variables were solved according to the maximum likelihood criterion, maximizing the probability of the random variables ϵ_v and ϵ_i. Since it was known that these variables have a Gaussian distribution, the maximum likelihood criterion was implemented by iterative application of the Gauss-Markov method.

The procedure started by assuming $\theta(t) = \phi(t) = 0$, from which the first approximation of $\psi(t)$ was calculated, using only vertical slit transits. Subsequently, the inclined slit equations were considered and a first approximation of $\theta(t)$ and $\phi(t)$ was obtained. The procedure was iterated until it converged to a stable solution.

The Gauss-Markov method allowed the estimated values of the unknown parameters and an estimate of the covariance matrix to be obtainied simultaneously, from which the standard deviation of the reconstructed attitude was computed for each observation frame. A simplified approach was adopted in order to reduce the computing time.

Time Segmentation and Model Selection

In normal conditions, i.e. in the absence of eclipses, occultations or other events disturbing the data, the long-term Fourier model was used. Intervals of a length close to a rotational period of the satellite were considered, starting and ending with a thruster firing. An overlap of at least one thruster firing interval between neighbouring solutions was used to avoid discontinuities in the attitude reconstruction. This was the preferred solution which was applied whenever possible, introducing occasionally large overlapping in order to allow this type of solution.

Occultation periods during which the thrusters were not fired could be included in the long-term model. When thruster firings took place during the occultation, then the data before and after the occultation could not be included in the same model. When, due to the presence of long occultations, it was not possible to select a time interval of the order of one satellite rotation (115–130 minutes), then, for intervals of a duration in the range of 30–115 minutes, the intermediate-term Fourier model was used.

When the satellite was in penumbra the short-term polynomial model in penumbra was imposed, interrupting the long- and intermediate-term models.

The short-term polynomial model was used only for single thruster firing intervals that could not be joined up with other time intervals.

Both polynomial models required a large number of degrees of freedom in consideration of the length of the time interval and they presented an estimation error larger than the one obtained by the Fourier model. Thus, they were used only in the case of penumbra or anomalous behaviour, when the application of the Fourier model could give non-negligible model errors.

Significance Test and Anomalous Situation Detection

The residuals for all observations were computed and subjected to a χ^2 test to assess the validity of the assumptions made: the goodness of the estimated variances of the measurement errors and the goodness of the parametric model used. Since the variances of the estimated star mapper transit time errors were very well assessed, the χ^2 test was mainly used to control the goodness of the attitude model, but it also allowed the star mapper data to be automatically rejected when the residuals were grossly inconsistent with its variance (as in the case of the observation of a wrong star or very erroneous star positions).

The χ^2 test permitted also the detection of situations in which the perturbing torque acting on the satellite had an anomalous behaviour. In such situations the short-term polynomial model was imposed, but this model was so general that it was rather suitable for any torque behaviour.

Table 7.3. Typical rounded *a posteriori* standard deviations expressed in mas obtained by the three attitude determination procedures. For OGARI, σ_ψ is obtained by the great-circle reduction.

Procedure	σ_ϕ	σ_θ	σ_ψ
OGARO	200	100	60
OGAR	60	30	15
OGARI	30	20	2

Convergence of the Iteration Process

The improvement of the attitude at different iterative stages was essentially due to two factors:

- each iteration involving either more observations or being just a re-iteration with the same data provided improved star positions for more and more stars (OGAR and OGARI);
- the determination of the attitude in ψ by the great-circle reduction permitted the assumption that this angle is perfectly determined so that only θ and ϕ remained to be computed, allowing them to be decorrelated from ψ (OGARI). In addition (see Section 6.1) its high precision meant that remaining transit time residuals reflected primarily the star mapper geometry corrections, which could therefore be calibrated, providing another means of improving the attitude.

The improvement obtained during this iterative procedure is illustrated by Table 7.3, which gives typical orders of magnitude of the *a posteriori* standard deviations for the three angles as obtained in the mean by each of the attitude determination procedures.

7.7. Performance Comparisons

A comparison of the reconstructed attitude results obtained by FAST and NDAC was carried out on suitably selected sets of reference great circles. The aim of the comparison was the assessment of the attitude reconstruction accuracy and the level of agreement between the results obtained by the two consortia, pointing out any unjustifiable disagreements. The comparison involved also results obtained with the great-circle reduction. The comparison was carried out along the following steps.

Preparation and Synchronization of the Data

The attitude reconstruction results produced by NDAC and FAST were expressed in different variables and referred to different celestial frames, as was described in the preceding sections. The attitude results were collected in data sets, describing the satellite axes positions and rotation rates for every observational frame. The criteria for accepting and deleting data were slightly different between the consortia, and gaps of different lengths occurred in the data. The first step in the comparison exercise was

therefore to synchronize the data, to extract a common sampling time set. Such a set contained typically 12 000 samples.

Differential Rotations

The reconstructed attitude can be represented by an orthonormal matrix, describing the attitude by the direction cosines of the equatorial coordinates at J2000 of the satellite (or instrumental) axes:

$$\mathbf{A}_j(i) = [\,\mathbf{x}_j(i)\ \mathbf{y}_j(i)\ \mathbf{z}_j(i)\,] \qquad [7.29]$$

where i denotes the sampling time instant and $j = 1, 2$ the two consortia.

The differences between the two sets of attitude data were expressed by 3-2-1 Euler angles, corresponding to the three rotations $\phi(i)$, $\theta(i)$, $\psi(i)$ through which $\mathbf{A}_2(i)$ was obtained from $\mathbf{A}_1$. The rotation vector $\mathbf{r}(i) = [\phi(i)\ \theta(i)\ \psi(i)]'$ described the attitude reconstruction differences with respect to the on-board instrumental reference frame, the satellite axes. The same difference can be expressed with respect to the celestial reference frame through the transformation:

$$\mathbf{r}_c(i) = \mathbf{A}\mathbf{r}(i) \qquad [7.30]$$

where $\mathbf{A}$ can refer to either $\mathbf{A}_1$ or $\mathbf{A}_2$ without any significant difference.

The differential rotation vector $\mathbf{r}(i)$ was decomposed as the sum of systematic and random differences. Two possible sources of systematic differential rotations were considered: the definitions of the celestial and the instrumental reference frames respectively.

The instrumental reference frame was defined by the star mapper geometry calibrations. Differences between the consortia in this calibration would cause a differential rotation that is constant in the instrumental reference frame. This constant rotation was denoted by the vector:

$$\mathbf{r}_0 = \begin{pmatrix} m_\phi \\ m_\theta \\ m_\psi \end{pmatrix} \qquad [7.31]$$

The celestial reference frame was defined by the positions of the star mapper stars as used in the attitude reconstruction. The two consortia determined and applied different corrections to the original Input Catalogue positions, resulting in slight differential rotations between the celestial reference frames used. This rotation was constant when expressed in celestial coordinates and described by the vector:

$$\mathbf{r}_{c0} = \begin{pmatrix} m_x \\ m_y \\ m_z \end{pmatrix} \qquad [7.32]$$

Thus, the differential rotation vector could be described by:

$$\mathbf{r}(i) = \mathbf{r}_0 + \mathbf{A}^{-1}(i)\mathbf{r}_{c0} + \mathbf{e}(i) \qquad [7.33]$$

where $\mathbf{e}(i)$ denotes the residual random term.

The systematic differential rotations could be estimated in principle by applying an ordinary least-squares method, but a collinearity problem arises, not allowing a rotation of the instrumental reference frame about the body z axis to be distinguished from a rotation of the celestial reference frame. Considering the fact that the calibration of the body reference frame with respect to rotation about the z axis was verified at the level of the great-circle reduction (see Chapter 9), it was assumed in the attitude comparison

that $m_\psi = 0$, leaving only the variables m_ϕ, m_θ, m_x, m_y, and m_z to be estimated by a Householder procedure.

Estimation of Variances

Once the estimated values were computed it was necessary to verify if the hypothesis that they were different from zero could be accepted, or if the resulting values were to be retained as incidental effects, produced by the random error $\mathbf{e}(i)$. Actually, while a statistical model for FAST attitude reconstruction was available, this was not the case for NDAC. So, an *a posteriori* approach was applied, based on the computation of the entropy of the signal $\mathbf{r}(i)$ (Donati & Sechi 1992). The distribution function equivalent number of the signal was computed and the separator thresholds were derived and used to establish the significance of the systematic components m_ϕ, m_θ, m_x, m_y, and m_z of $\mathbf{r}(i)$ obtained by applying the least-squares method to the system of equations (Equation 7.33).

Global Evaluation of the Standard Deviations

Then, modelling $\mathbf{r}(i)$ by a second order stochastic process with a uniform distribution of energy in a suitable orthogonal basis of dimension equal to the already evaluated equivalent number of degrees of freedom, the standard deviations of these components were evaluated:

$$\boldsymbol{\sigma} = \begin{pmatrix} \sigma_\phi \\ \sigma_\theta \\ \sigma_\psi \end{pmatrix} \qquad [7.34]$$

Denoting by σ_{1q} and σ_{2q} the standard deviations of the two attitude reconstructions to be compared, in any of the angles ($q = \phi$, θ or ψ), the following holds:

$$\sigma_q^2 = \sigma_{1q}^2 + \sigma_{2q}^2 - 2\rho\sigma_{1q}\sigma_{2q} \qquad [7.35]$$

where ρ is the correlation coefficient between the two realisations of the attitude. The correlation is close to +1 because both are obtained from the same star mapper observations and their Poisson noise. Given σ_{1q} and σ_{2q}, this relation allowed the construction of a test of the hypothesis that both attitude reconstructions were within given limits. This had to be satisfied for an acceptable value of ρ. The test could, of course, not exclude that both reconstructions were affected by some large correlated errors.

Results of the Last Attitude Comparison

The last attitude comparison was carried out on a set of 24 orbits chosen among those having some critical problems such as spin-up of the redundant gyro, redundant gyro running, well covered eclipse, reference great-circle pole close to the ecliptic plane, strong perturbing torques.

Systematic differences were found both in the instrumental and in the celestial reference frames. The first were explained by some differences in the star mapper calibrations, and the second by differences in the celestial reference frames adopted by the consortia. These differences were taken into account by the catalogue merging procedure. Assuming that the term m_ψ is negligible since it was determined by the great-circle reduction, the effects in each frame were evaluated. The results are presented in Table 7.4. In

Table 7.4. Estimated values and standard deviations of the rotation components, expressed in mas.

Component	Estimate (mas)
m_ϕ	-12 ± 14
m_θ	$+98 \pm 23$
m_x	$+15 \pm 6$
m_y	$+17 \pm 6$
m_z	-13 ± 5

Table 7.5. Estimated standard deviations of the random terms in the differential rotation in body axes, expressed in mas. Column (a): all frames included; (b): excluding outliers, i.e. random terms exceeding $\pm 3\sigma$.

Component	Estimates (mas)	
	(a)	(b)
σ_ϕ	129 ± 90	82 ± 24
σ_θ	81 ± 47	54 ± 14
σ_ψ	12 ± 10	3 ± 3

addition, Table 7.5 shows the standard deviations σ_q of the components ($q = \phi, \theta, \psi$) of the differential random rotation $\mathbf{e}(i)$ along with their estimated standard deviations σ_{σ_q}.

The results shown in Tables 7.4 and 7.5 correspond to the most difficult cases, presumably subject to the largest errors. However, in normal cases found in the great majority of great circles, they happen to be also comparable to the figures given in Table 7.3. The interpretation is that attitude reconstructions made in both consortia show a general agreement which is of the order of the requirements and is sufficient to avoid the introduction of significant differences in the results of the great-circle reduction—the primary objective of the attitude determination activities. The uncertainties in the final NDAC attitude were in addition estimated in the Tycho data reductions as being at least 7 mas along scan and 30 mas perpendicular to the scan, much better than the 100 mas expected before launch for the latter quantity.

F. van Leeuwen, F. Donati, J. Kovalevsky